Earth Systems and Environment
https://doi.org/10.1007/s41748-025-00952-0

ORIGINAL ARTICLE

A Novel Cost-Effective Approach for Collecting Time-Series of Turbulence Properties in Aquatic Systems - Part I

Fahad Al Senafi[1] · Ayal Anis[2] · Tariq Al Rushaid[1] · Sebastiano Piccolroaz[3]

Received: 11 February 2025 / Revised: 9 November 2025 / Accepted: 13 November 2025

Abstract

This study examines the impact of winter Shamal events (strong northwesterly winds that commonly generate significant dust storms) on water column mixing and turbulence in the northern Arabian Gulf using a newly developed method for computing turbulence properties, specifically turbulent kinetic energy dissipation rates (ϵ) and temperature variance dissipation rates (χ_T). Fast-response temperature sensors were employed during November 2023 to capture detailed time-series measurements during both Shamal and pre-Shamal periods. The results demonstrate that Shamal-induced turbulence significantly enhances air-sea exchanges of momentum and heat, driving intense wind-induced mixing and convective processes. These processes led to a sharp increase in ϵ and χ_T, particularly during the peak of the Shamal event, where ϵ values ranged from 10^{-6} to 10^{-4} W/kg. Based on our results from comparison of turbulence parameters during periods of different physical forcings (wind stress and convection), we suggest that moored, affordable, fast-response temperature sensors can deliver time-series estimates of ϵ and χ_T with a higher degree of reliability, showing deviations of less than 18% compared to a benchmark turbulence profiler used to corroborate the newly developed method. This capability is particularly significant, as this study represents one of the first observational analysis of water column turbulence in response to Shamal events, offering valuable insights into the Gulf's broader hydrodynamics. These findings enhance our understanding of Shamal-driven mixing processes and introduce an innovative method for measuring turbulence, with broader implications for the study of ocean mixing in coastal and semi-enclosed seas.

✉ Fahad Al Senafi
fahad.alsenafi@ku.edu.kw

[1] Department of Marine Science, College of Science, Kuwait University, Kuwait City, Kuwait

[2] Department of Oceanography , Texas A&M University , College Station, TX, USA

[3] Department of Civil Environmental and Mechanical Engineering , University of Trento , Trento, Italy

Published online: 12 December 2025

Graphical Abstract

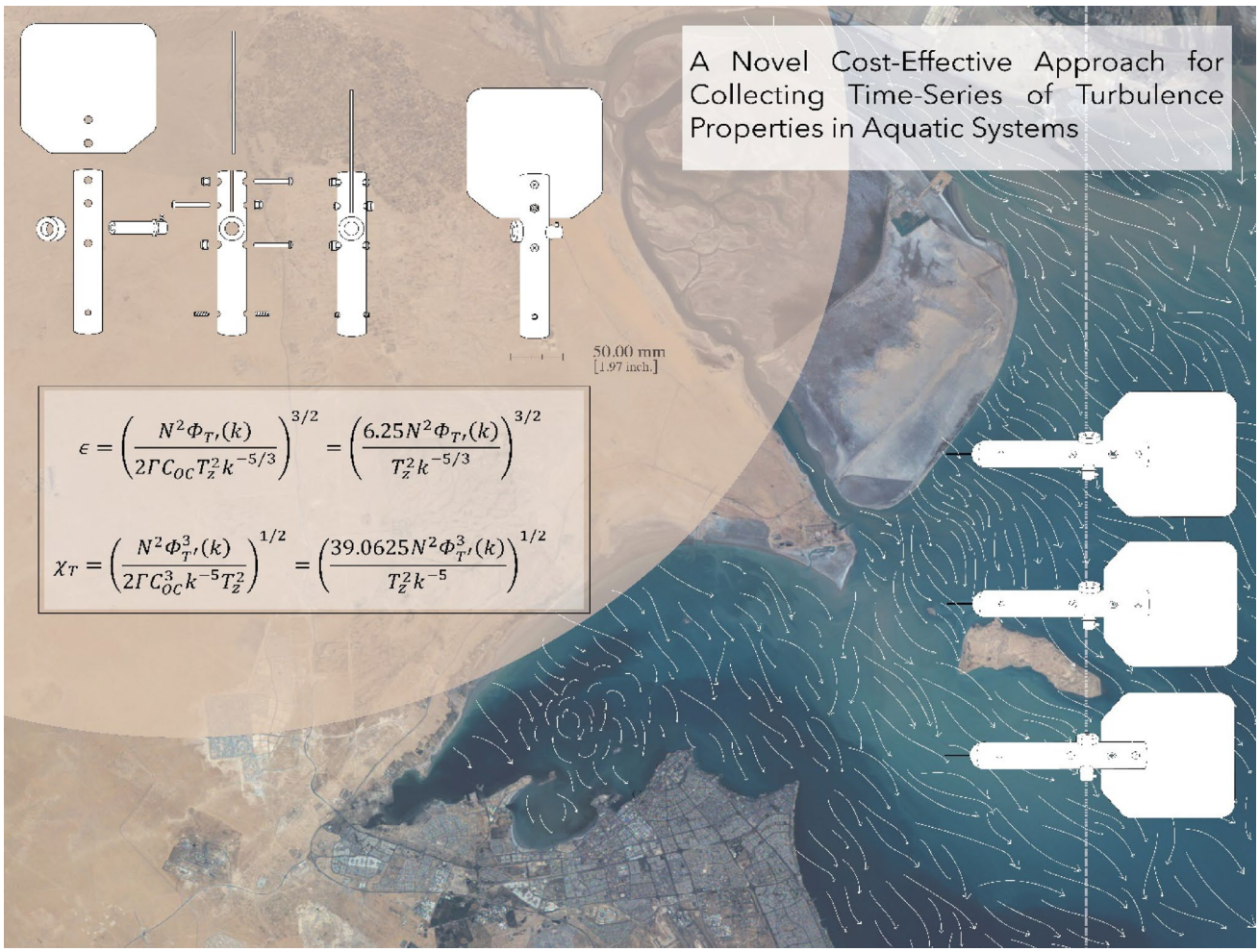

Highlights

- A novel method for computing turbulence properties using moored, affordable fast-response temperature sensors was successfully applied.
- Detailed time-series observations of hydrographic and turbulence parameters were obtained during winter Shamal events in the northern Arabian Gulf.
- Winter Shamal events induced significant increases in water column mixing, driven by strong wind forcing and surface heat fluxes.
- This study provides the first observational analysis of Shamal-induced water column mixing intensities.

Keywords Air-Sea interaction · Arabian gulf · Buoyancy-Driven and Wind-Driven convection · Shamal (Strong northwesterly winds in the arabian gulf) · Surface boundary layer turbulence

1 Introduction

The Arabian/Persian Gulf (hereafter referred to as the Gulf) lies within the subtropical high-pressure belt (25–30°N), a region characterized by some of the harshest desert conditions on Earth (Brook et al. 2006). The descending dry air creates arid desert conditions, while the Gulf is also influenced by extra-tropical weather systems from the northwest. One of the most significant meteorological phenomena affecting the Gulf is the Shamal wind (Blain 2000). Shamal ("north" in Arabic) refers to strong northwesterly winds that occur primarily in summer (June to August), driven by the relative strengths of the Indian and Arabian thermal lows, and in winter (November to March), driven by synoptic weather

systems from the northwest (Aboobacker et al. 2011). These winds can intensify into "Shamal Events," which often transport dust from the Mesopotamian floodplain, significantly reducing visibility across the eastern and southern Arabian Peninsula and Iran (Abdi Vishkaee et al. 2012). On average, approximately ten Shamal events occur annually, with significant impacts on both the natural environment and human health (Al Senafi and Anis 2015).

Winter Shamal events, in particular, are highly impactful, bringing cold, dry air masses that trigger abrupt changes in the Gulf's circulation, mixing intensities, and heat budget (Li et al. 2020a). Similar to the Mistral winds in the Gulf of Lion in the Mediterranean (Keller et al. 2024) and the Bora winds in the Adriatic Sea (Lee et al. 2005), Shamal winds can induce intense wind-driven mechanical mixing, convective cooling, and overturning processes. The surface forcing generated by Shamal events—through buoyancy, momentum, and heat fluxes—likely plays a crucial role in the formation and location of Gulf Deep Water (GDW), which eventually spills into the Indian Ocean (Swift and Bower 2003).

The characteristics of Shamal events vary significantly by season. Summer Shamals can last for several weeks, bringing extreme heat up to 50 °C and sustained winds of up to 13 m/s (Rao et al. 2003), while winter Shamals typically last between 2 and 5 days, delivering cold air masses and stronger winds that can reach up to 20 m/s (Rao et al. 2001). These short but intense events can rapidly alter surface circulation and sea surface temperatures (SSTs) over periods ranging from days to weeks (Al Senafi and Anis 2020a).

Despite the significance of Shamal events, the air-sea dynamics of the Gulf remain poorly understood, largely due to the scarcity of oceanographic and meteorological measurements. No observational study has closely examined the response to Shamal events and their effects on water column mixing intensities. Understanding these effects is critical, as turbulence plays a key role in determining transport pathways within the marine environment, as well as in mediating air-sea exchanges of momentum, heat, and gases (Bruciaferri et al. 2022). In particular, quantifying the transport and dispersion of nutrients—which sustain ecological systems but may also trigger harmful algal blooms (e.g., Sullivan et al. 2003)—along with other water-borne substances such as oil and its derivatives (e.g., Yang et al. 2015), sewage (e.g., Ragessi et al. 2022), and pollutants (e.g., Sutherland et al. 2023), as well as sediments in the coastal ocean (e.g., Cheng et al., 2020), remains a pressing challenge in oceanography. These processes are driven by turbulent mixing and circulation patterns, making it essential to understand the role of Shamal events in shaping the fate of all such water-borne substances. Improved knowledge of these dynamics is crucial for predicting the environmental impacts both positive and negative on marine ecosystems and natural resources (Ben-Hasan et al. 2018; Fieseler et al. 2023; Ben-Hasan 2024). Furthermore, such understanding is essential for anticipating the effects of global climate change on air-sea temperature dynamics (Attrill 2009; Al Senafi et al. 2024), as well as on the frequency and severity of droughts (van Vliet et al. 2013), flooding (Mirza 2002), and extreme weather events such as the Shamal itself (Al Senafi and Anis 2015).

To address these challenges, we conducted a study aimed at enhancing the understanding and quantification of mixing processes and the related fluxes of water-borne substances in the northern Gulf, as well as their relationship to external forcing. Our primary focus was on processes driven by winter Shamal events, which are key drivers of turbulence, mixing, mass fluxes, and dispersion in this region. The study employed detailed time-series measurements of hydrographic and turbulence parameters, obtained using a turbulence profiler in conjunction with a newly developed method incorporating fast-response temperature sensors, as detailed in Sect. 2. A key innovation of this method was the deployment of these fast-response temperature sensors on freely rotating wings, allowing them to align with the flow and minimize wake interference. This design optimized sensor exposure to ambient turbulence while reducing measurement distortions, ensuring high-fidelity data collection. These turbulence measurements were further complemented by simultaneous surface meteorological data, enabling the computation of surface forcing, including momentum, buoyancy, and heat fluxes. The analysis and results of these measurements are discussed in Sect. 3, with conclusions and future directions outlined in Sect. 4.

2 Methodology

To capture the flow, thermal, and turbulence fields, we chose a site near Qarooh Island, Kuwait (28˚48.9730 N, 048˚46.457' E; Fig. 1). The site, located 44 km east of Kuwait's mainland and 120 km south of the Euphrates-Tigris delta, was selected for its 30.4 m depth, being the deepest local area, and its distance from possible obstructions to the dominant northwesterly Shamal and southeasterly winds, both of which are the focus of this study (Fig. 1). For our field campaign we used two approaches: The first involved a month-long deployment in November 2023, during which we established a comprehensive suite of meteorological sensors mounted on a mast at the pier on Qarooh Island (Sect. 2.1). Additionally, we deployed a string of temperature sensors along a tight mooring line, the bottom weight of which was connected via a lead line to a bottom-mounted Nortek Signature Series 1 MHz Acoustic Doppler

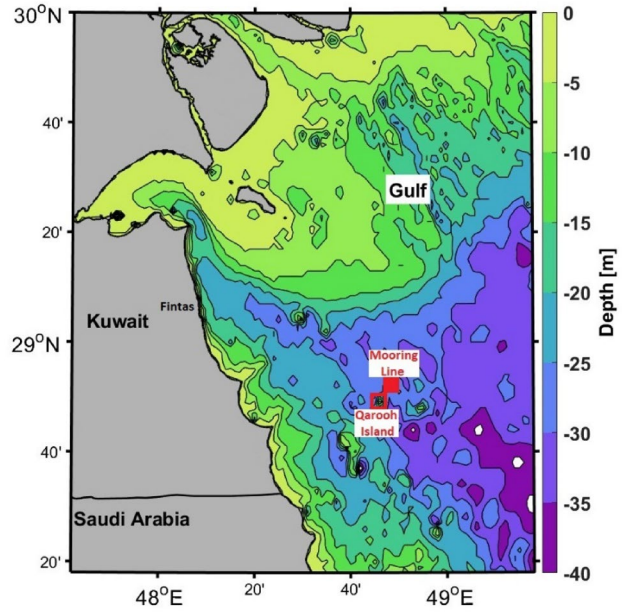

Fig. 1 Schematic of the experiment location off Qarooh Island, Kuwait. Map showing the bottom topography (color) and mooring site (filled red squares). Depth contours are in 5 m intervals

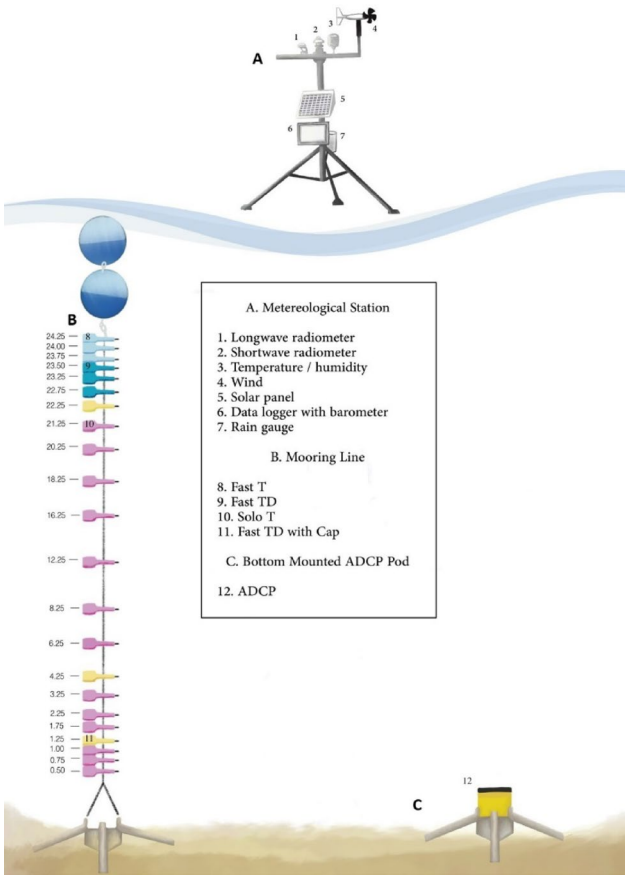

Fig. 2 Schematic of the experiment setup showing the (**A**) meteorological station (**B**) mooring line (**C**) bottom mounted ADCP pod

Current Profiler (ADCP) positioned 25 m away at a depth of 30.4 m (Fig. 2), 3.14 km northeast of the island (Sect. 2.2). The ADCP recorded current profiles at 1.5-minute intervals with a vertical resolution of 0.5 m bins, spanning up to 30 m above bottom (MAB), with a blanking distance of 0.2 m, totaling 60 cells. The raw velocity data were quality controlled, and measurements with signal strength less than 3 dB above background noise were discarded.

The second approach focused on continuous profiling over a four-day period, using a turbulence profiler to capture the multiscale energy cascade, down to the scale of molecular viscosity, at a location within 1 km of the mooring line (Sect. 2.3). Details of the instruments, measurements, and methods used in this study are described in the following sections.

2.1 Surface Meteorology

A complete suite of meteorological sensors provided continuous measurements of air temperature and humidity (HygroVUE 5; installed in a fan aspirated solar radiation shield), wind speed and direction (Young marine wind monitor 05106), incoming shortwave (Hukseflux SR11) and longwave radiation (Hukseflux IR02), rainfall (Texas electronic 525), and barometric pressure (Setra 278) (Fig. 2A). Sensors were mounted at a nominal distance of 4.13 m above sea level (ASL) and sampled every 5 s. Data was then averaged and logged in 1 min intervals on a datalogger (Campbell CR6). From these data, the surface wind stress, τ_o, and the net surface heat flux, J_q^o, were computed using the Coupled Ocean Atmosphere Response Experiment formulation (COARE version 3.5; Fairall et al. 1996, 2003). The air-sea fluxes allowed us to compute the classical Monin-Obukhov length scale, L, to assess the relative importance of wind stress (L >0) versus buoyancy forces (L < 0) on upper ocean mixing, particularly during events like Shamals

$$L = \frac{-u_*^3}{\kappa\ J_b^o}, \tag{1}$$

where $u_* = \sqrt{\tau_o/\rho_w}$ is the surface friction velocity (τ_o wind stress and ρ_w is the seawater density), $\kappa = 0.4$ is the von Karman's constant. The surface buoyancy flux, J_b^o, given by $J_b^o = -g\alpha\, J_q^o/(C_p\,\rho_w)$, where g is the gravitational acceleration, α is the thermal expansion coefficient for water, and C_p is the specific heat capacity of sea water (Monin and Obukhov 1954; Anis 2006).

2.2 Mooring Line

2.2.1 Design& Setup

A string of 22 temperature-depth (TD) sensors were deployed along the mooring line. These sensors provided high temporal (up to 16 Hz) and vertical resolution temperature profiles (0.25 m to 4 m), allowing for detailed investigation of turbulent processes during both calm and energetic atmospheric events. Instruments near the surface and bottom boundary layers were spaced at 0.25 m increments, with spacing gradually increasing toward the mid-layer (Fig. 2B).

The compact RBR*solo*³ T and RBR*duet*³ T.D loggers (RBR Ltd.) used in this study were chosen due to their relatively low cost, compact size (~240 mm long, ~25 mm diameter), lightweight design (120 g in air, 20 g in water), fast sampling rates (2 Hz for standard models, 16 Hz for fast models), high accuracy (±0.002 °C) and resolution (<0.00005 °C). These thermistors have a response time constant (time it takes to reach 63% of the final value, the e-folding time; Emery and Thomson 2004) of 70 ms and 700 ms, respectively, for fast and standard. The transfer function of these thermistors is modeled as a single-pole system, which attenuates energy at higher frequencies while still allowing high-frequency signals to pass with some attenuation (20 dB/decade) (Gregg and Meagher 1980; Nash et al. 1999; Tagawa et al. 2003). This fast response enables the RBR*solo*³ T sensors to effectively capture rapid temperature changes such as those associated with turbulence.

All loggers were mounted on a Delrin frame, equipped with a rudder that was designed, cut, and fabricated in our lab, allowing them to rotate freely and orient the sensor tip into the flow to minimize disturbances. To avoid wake generation and potential contamination of temperature measurements, the original plastic sensor guards were removed. Additionally, the frame and rudders were coated with antifouling paint to minimize biofouling. All temperature loggers used in this study were recalibrated by the manufacturer prior to deployment.

2.2.2 Data Processing

Processing of the measured temperature time series began with trimming periods when the sensors were out of the water, followed by despiking the data. Power spectral density (PSD) estimates were computed for segments of 1024 data points for standard RBR*solo*³ T models and 8192 for fast models, corresponding to approximately 8.5 min of data. The 8.5 min segment duration was chosen to closely match the profiling interval of the MicroCTD, which completed one profile approximately every 4 to 10 min depending on water depth. This alignment enabled synchronized comparisons between temperature-based turbulence estimates and shear-probe-derived estimates from the MicroCTD. The resulting data were then used to estimate turbulent kinetic energy dissipation rates (ϵ) and temperature variance dissipation rates (χ_T) using well-established methods (e.g. Hill 1978; Kerr 1990; Sreenivasan 1996; Kundu and Cohen 2012; Portwood et al. 2022).

To provide conceptual clarity, it is helpful to consider that in turbulent flows, temperature behaves as a passive scalar, meaning it is transported and mixed by the flow without strongly influencing it. The fine-scale structure of the temperature field reflects the underlying turbulent kinetic energy, as energy cascades from larger to smaller eddies, leading to enhanced mixing and temperature fluctuations at small scales. These fluctuations, when analyzed in spectral space, provide a means to infer both how rapidly turbulence is dissipating (via ϵ) and how temperature variance is smoothed by molecular diffusion (via χ_T).

The rate of dissipation of temperature variance is given by:

$$\chi_T = 2D\langle(\nabla T')^2\rangle \tag{2}$$

where $T\prime$ are the molecular temperature, $\nabla T'$ is the spatial gradient of the temperature fluctuation, and D is the thermal diffusivity. The operator $\langle\cdot\rangle$ indicates averaging, hence the term $\langle(\nabla T')^2\rangle$ is the variance of the gradient of the fluctuating temperature field. In case of isotropic turbulence, Eq. (2) can be written in terms of the gradient along the longitudinal direction x as:

$$\chi_T = 6D\langle\left(\frac{\partial T'}{\partial x}\right)^2\rangle \quad . \tag{3A}$$

In wavenumber (k) space, the temperature variance dissipation rate is expressed as:

$$\chi_T = 6D\int_0^\infty \Phi_{T\prime x}(k)\,dk \tag{3B}$$

where $\Phi_{T\prime_x}$ is the spectrum of $T'_x = \partial T'/\partial x = (1/u)(\partial T'/\partial t)$, using Taylor's frozen flow hypothesis with the mean speed, u, of the oncoming flow provided by the ADCP to convert the time-domain signal into spatial signal, and k is the cyclic longitudinal wavenumber with units of cycle per meter (cpm).

The vertical eddy diffusivity, K_T, for heat (Osborn and Cox 1972) can be estimated as:

$$K_T = \frac{\chi_T}{2T_z^2} \tag{4}$$

where T_Z is the mean vertical temperature gradient.

For steady-state turbulence, where turbulence kinetic energy dissipation rate is balanced by shear production (mechanical) and buoyancy production, J_b^o, the eddy diffusivity for density, K_ρ, can be estimated as:

$$K_\rho = \frac{\Gamma\ \epsilon}{N^2} \tag{5}$$

where $\Gamma = 0.2$ is the mixing efficiency, and N is the buoyancy frequency (Osborn 1980). The buoyancy frequency was computed under the assumption of a constant salinity profile, as the haline contribution to both stratification and surface buoyancy flux was consistently minor, accounting for approximately 22% of the observed density variability and less than 30% of the surface buoyancy flux, during the study period. This assumption is supported by salinity measurements from the MicroCTD turbulence profiler, which showed that temperature dominated the density stratification signal across the record. Since the moored temperature array did not include conductivity sensors, density and buoyancy frequency at that site were estimated from temperature alone.

Assuming $K_T = K_\rho$, and using Eqs. (4) and (5) we derive the following expression for ϵ:

$$\epsilon = \frac{N^2 \chi_T}{2\Gamma T_z^2}\ . \tag{6}$$

The mean-square turbulence temperature fluctuations (i.e. the variance) in the longitudinal, x, direction can be expressed as:

$$\langle T'^2 \rangle = \int_0^\infty \Phi_{T\prime}(k)\, dk \tag{7}$$

where, $\varphi_{T\prime}$ is the one-dimensional spectral density of the temperature fluctuations, $T\prime$. In the inertial-convective range, dimensional analysis (e.g. Sreenivasan 1996; Danaila and Antonia 2009) relates $\Phi_{T\prime}(k)$ to k as:

$$\Phi_{T\prime}(k) = C_{OC}\epsilon^{-1/3}\chi_T k^{-5/3} \tag{8}$$

where $C_{oc} = 0.4$ is the Obukhov-Corrsin constant (Sreenivasan 1995). If temperature fluctuation measurements yield well-resolved spectra in the inertial-convective range, the spectra should follow a −5/3 slope in log-log space. Normalizing the spectra with $C_{oc}k^{-5/3}$ gives:

$$\frac{\Phi_{T\prime}(k)}{C_{OC}k^{-5/3}} = \epsilon^{-1/3}\chi_T \tag{9}$$

where, for some arbitrary spectra the right-hand-side is a constant combining the TKE and temperature variance dissipation rates in the inertial-convective range. Rearranging Eq. (6) results in a second expression that combines ϵ and χ_T:

$$\frac{N^2}{2\Gamma T_z^2} = \epsilon\chi_T^{-1}\ . \tag{10}$$

Multiplying Eqs. (9) and (10) allow the computation of ϵ and χ_T:

$$\epsilon = \left(\frac{N^2\Phi_{T\prime}(k)}{2\Gamma C_{OC}T_z^2 k^{-5/3}}\right)^{3/2} = \left(\frac{6.25N^2\Phi_{T\prime}(k)}{T_z^2 k^{-5/3}}\right)^{3/2} \tag{11}$$

where the numerical factor 6.25 results from using Γ and C_{OC}. Solving for χ_T results in:

$$\chi_T = \left(\frac{N^2\Phi^3_{T'}(k)}{2\Gamma C_{OC}^3 k^{-5}T_z^2}\right)^{1/2} = \left(\frac{39.0625N^2\Phi^3_{T'}(k)}{T_z^2 k^{-5}}\right)^{1/2}\ . \tag{12}$$

To summarize, the discrete vertical profiles acquired from the thermistor string were utilized to evaluate N^2 and T_z^2, while data from individual thermistors were analyzed to compute $\Phi^3_{T'}$, enabling the estimation of ϵ and χ_T at the corresponding thermistor depths, as described by Eqs. (11) and (12).

We note that while the use of high-frequency temperature measurements for turbulence studies is well established, particularly through moored FP07 thermistors that record the time derivative of temperature fluctuations (dT′/dt), as demonstrated in the work of Moum and Nash (2009), our approach is distinct. Instead of FP07 sensors, we employ compact, off-the-shelf RBRsolo³ T loggers that directly measure temperature fluctuations (T′), enabling a cost-effective and easily deployable alternative for long-term moored observations.

2.2.3 White Noise and Sensor Performance Validation

White noise introduced by the electronic circuits of the sensors was modeled as broadband white noise. This noise, characterized by levels between 1.05×10^{-9} and 8.11×10^{-9} °C²/Hz, was incorporated into the spectral analysis to account for its influence at high frequencies. Although the thermistors may exhibit a $1/f$ noise component at lower frequencies, this contribution is typically minimal because the temperature signals at these frequencies are much larger in magnitude, effectively dominating over the noise (Halverson

et al. 2017). To evaluate the accuracy of the moored temperature time series, we conducted a direct comparison with temperature profiles obtained from the MicroCTD profiler. For each of the 18 RBRsolo³ T sensors, we extracted the nearest corresponding depth from the MicroCTD casts during the 15–18 November period. The comparison showed strong agreement across all depths, with significant correlation coefficients exceeding 0.77 (Fig. 3). This validation demonstrates the consistency of the moored sensors with the profiler data and supports the reliability of the moored temperature measurements.

2.3 Turbulence Profiling

Microstructure data were collected using the Rockland Scientific International (RSI) MicroCTD, a profiler specifically designed for turbulence measurements in shallow coastal environments. The instrument was deployed in the water column, capturing profiles from approximately 1 m below the surface to 0.1 m above the seabed at intervals of 4–10 min, depending on water depth. All collected data were stored internally and later retrieved for analysis.

The MicroCTD profiler, approximately 1 m in length, is equipped with two microstructure airfoil shear probes and two FP07 fast-response thermistors, all sampling at 512 Hz. The airfoil probes are positioned orthogonally to measure both components of horizontal velocity shear fluctuations, $\partial u' / \partial z$ and $\partial v' / \partial z$. The instrument also includes piezoelectric accelerometers that record at 512 Hz to identify and remove vibrations that might contaminate the shear probe signals. Additionally, the profiler is equipped with a precision conductivity-temperature-depth (CTD) sensor and a pressure transducer, both operating at 64 Hz.

Raw turbulence signals were processed using a customized version of RSI's ODAS v4.4 libraries, following adaptations detailed in Piccolroaz et al. (2021). The calibration sensitivities of the shear probes were used to convert raw signals into physical units, while the temperature sensors were benchmarked against high-precision temperature measurements. Vertical profiles were segmented into overlapping 2-meter intervals, with each segment further subdivided into five 50% overlapping subsegments. PSD estimates for both shear and temperature gradient signals were computed by applying Welch's method with detrending and Hanning windowing, ensuring a smoothed spectral representation of turbulence within each segment.

Taylor's frozen turbulence hypothesis was applied to convert frequency spectra into wavenumber spectra using the profiler's fall speed, estimated from the differentiated pressure time series. To enhance data quality, the shear probe signals underwent spike removal, and low-frequency components linked to profiler motion were filtered out. Corrections for spatial attenuation effects and high-frequency noise contamination were applied, utilizing data from onboard accelerometers. Similarly, temperature gradient spectra were corrected for sensor response using a single-pole transfer function, compensating for the FP07 thermistor's nominal 7 ms time constant.

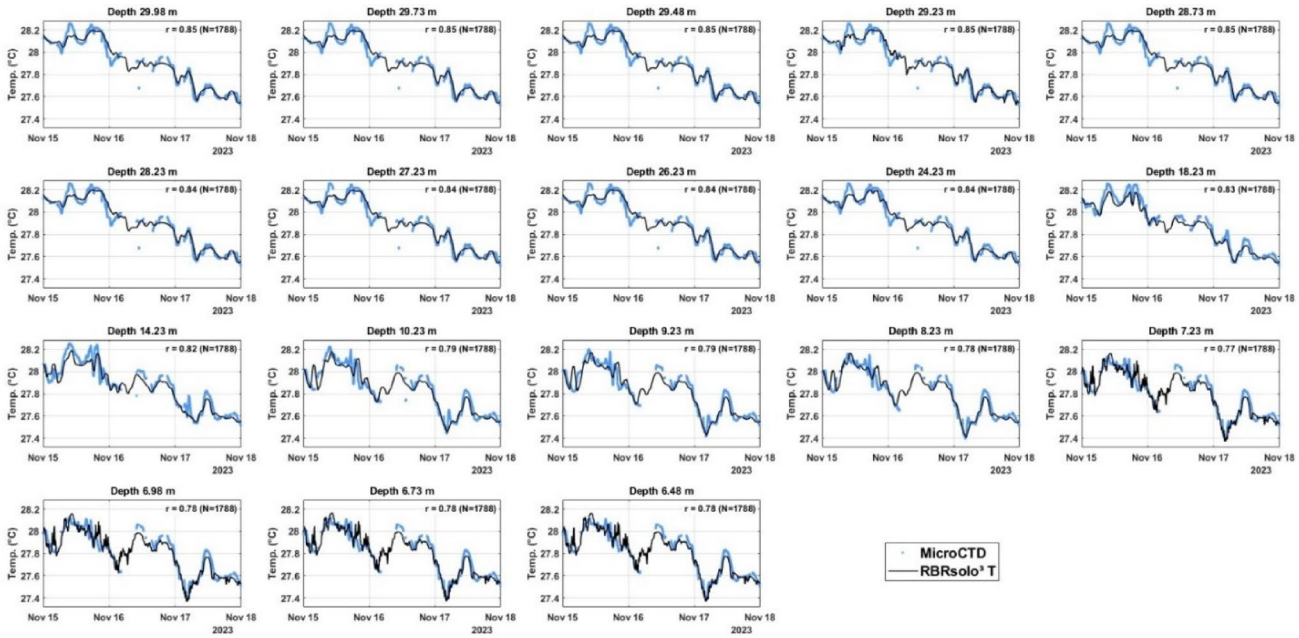

Fig. 3 Time series comparison between 18 RBRsolo³ T sensors (black lines) and corresponding MicroCTD temperature measurements (blue dots) extracted at the nearest depth for each profile. Each subplot corresponds to a distinct RBRsolo³ T sensor located at specific depth intervals from 6.23 m to 29.98 m. The correlation coefficient and number of samples are noted in the upper-right of each panel

The processed wavenumber spectra for shear and temperature gradients were used to estimate the dissipation rates of turbulent kinetic energy, ϵ and temperature variance χ_T. Under the assumption of isotropic turbulence, ϵ was determined using:

$$\epsilon = \frac{15}{2}\nu \left\langle \left(\frac{\partial u'}{\partial z} \right)^2 \right\rangle = \frac{15}{2}\nu \int_0^\infty \psi_{u'_z}(k)\, dk, \tag{13}$$

where ν is the kinematic viscosity of seawater, $\psi_{u'_z}(k)$ represents the shear wavenumber spectrum, and the integral spans the resolved lower and upper bounds wavenumber range $[k_L, k_U]$. The initial estimate of ϵ was corrected for unresolved variance using the empirical Nasmyth spectrum, following the methodology outlined in Piccolroaz et al. (2021).

Similarly, the dissipation rate of temperature variance (χ_T) (see Equations (3A)-(3B)), was computed as:

$$\chi_T = 6D\left\langle \left(\frac{\partial T'}{\partial x} \right)^2 \right\rangle = 6D \int_0^\infty \Phi_{T'_z}(k)\, dk, \tag{14}$$

where $\Phi_{T'_z}(k)$ is the wavenumber spectrum of temperature gradient fluctuations. The Kraichnan theoretical spectrum (Kraichnan 1968) was fitted to the observed spectrum using the maximum likelihood estimation (MLE) method described by Ruddick et al. (2000). This procedure provided an alternative estimate of both for χ_T and ϵ. The iterative fitting approach accounted for sensor noise, and only high-quality estimates were retained based on established criteria such as goodness-of-fit, signal-to-noise ratio, and sufficient spectral resolution. A more detailed description of the microstructure data processing methodology and quality metrics used is provided in Ruddick et al. (2000) and Piccolroaz et al. (2021).

3 Results & Discussion

In this section, we examine and discuss how the atmospheric conditions and air-sea fluxes during three distinct phases: (Sect. 3.1) calm conditions, (Sect. 3.2) a pre-Shamal phase characterized by southeasterly winds, and (Sect. 3.3) a Shamal event, marked by strong northwesterly winds influenced the thermal structure of the water column from November 14th to November 19th, 2023. The analysis covers both air-sea heat and momentum fluxes as well as the thermal response of the water column, with a particular focus on the impact of atmospheric forcing on vertical mixing and stratification.

3.1 Calm Period (Midnight To Evening of November 14th)

3.1.1 Atmospheric Conditions and Surface Fluxes

The calm period, defined from midnight (00:00) of November 14th to the early evening of that day (17:30), was characterized by weak wind speeds less than 2.5 m/s and wind stress close to 0 N/m² throughout this time (Figs. 3A and 4A). These conditions resulted in very little mechanical energy available for turbulent air-sea interactions. With such low winds, the atmosphere exerted limited influence over the ocean surface, contributing to stable initial hydrographic conditions that will be discussed in detail below.

Barometric pressure remained relatively steady at around 1014–1016 mb (Fig. 4B), reflecting the absence of significant weather systems or pressure gradients in the region. The latent heat flux, which represents the energy lost from the ocean via evaporation, dropped from a peak of 266 W/m² to near-zero towards the end of the period (Fig. 5E). These limited evaporation rates were due to weak winds and higher air humidity of 64% (Fig. 4D), restricting moisture transport away from the ocean surface. Similarly, the sensible heat flux, which accounts for heat exchange due to temperature differences between the air and sea, was negligible, with values less than 10 W/m² (Fig. 5D), as air-sea temperature contrasts averaged only 1.7 °C (Fig. 4C).

The net heat flux was negative during daytime (Fig. 5F; red), indicating that the ocean was absorbing heat, primarily (73%) from shortwave solar radiation (Fig. 5B), as clear skies likely dominated during this period. This clear-sky condition is indicated by the well-defined bell-shaped solar radiation pattern, allowing the SST to warm up to 0.8 °C. The lack of wind-driven cooling processes combined with the warmer air temperature than sea (Fig. 4C) maintained this heat gain at the surface. However, after sunset, the net heat flux turned positive (Fig. 5F; blue), suggesting heat loss. This diurnal cycle of heating and cooling contributed to minimal overall air-sea heat exchange, with a period-average net heat flux of 48 W/m² which is about a fifth of the heat loss observed during the following phases.

3.1.2 Water Column Thermal Structure & Stability

During the calm period, the initial water column exhibited a persistent, relatively strong stratified thermal structure, as indicated by the temperature contour plot and temperature traces (Fig. 6). Surface temperatures were around 28.2 °C, with a gradual cooling gradient extending towards the seabed, where temperatures were approximately 27.9 °C (Fig. 6A). The well-separated temperature traces throughout most of the period indicate the presence of a relatively

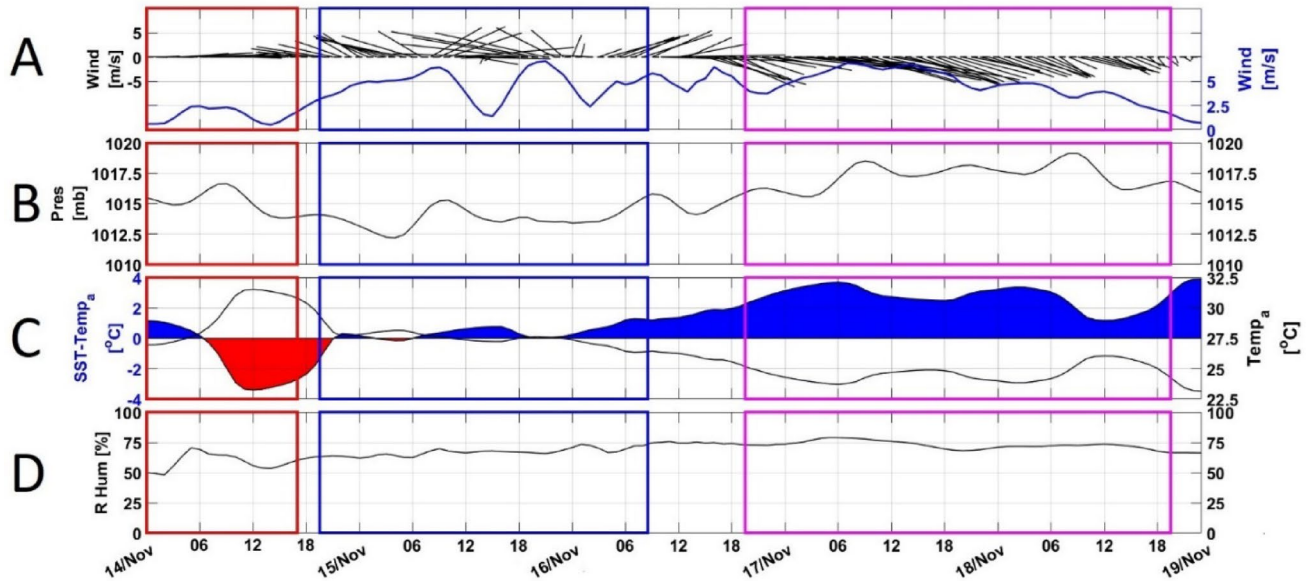

Fig. 4 Surface meteorological parameters from 14 to 19 November 2023, displayed from top to bottom: (**A**) wind speed (in blue) and hourly wind vectors, (**B**) barometric pressure, (**C**) air temperature (in black) and the temperature difference between air and sea surface temperatures (shown with blue-red shading), and (**D**) relative humidity. The periods of calm, pre-Shamal, and Shamal are indicated by red, blue, and magenta boxes, respectively. No rainfall was measured during this period; thus, rainfall data is not included in the figure

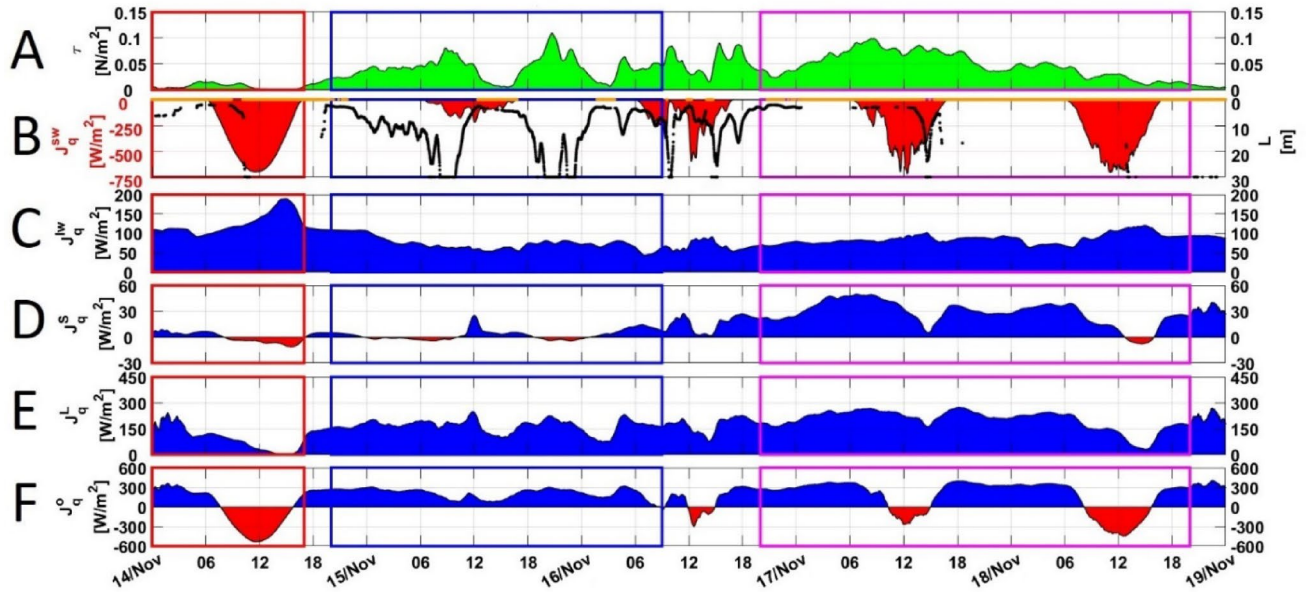

Fig. 5 Surface Heat and Momentum Fluxes from 14 to 19 November: (**A**) wind stress, (**B**) short-wave radiation and Monin-Obukhov length scales with positive values of the Monin-Obukhov length are shown in black, while negative values and those less than 2 m are shown in orange and set to zero. (**C**) long-wave radiation, (**D**) sensible heat flux, (**E**) latent heat flux, and (**F**) net heat flux. In panels (**B**) through (**F**), blue shading indicates positive heat flux values representing heat loss from the sea, while red shading indicates negative values, representing heat gain by the sea. Red, blue, and magenta boxes mark the periods of calm, pre-Shamal, and Shamal, respectively

stratified water column (Fig. 6B). The warm surface sensors (depicted in red and orange) are clearly separated from the cooler deeper sensors (depicted in green and blue). This lack of convergence between the temperature traces implies weak vertical mixing, consistent with the calm atmospheric conditions. As highlighted above, the surface waters experienced atmospheric heating towards midday in response to solar radiation as well as air-sea temperature contrast (Fig. 4C; red), but the deeper layers remained largely unaffected during this morning time, as indicated by the temperature vertical profiles.

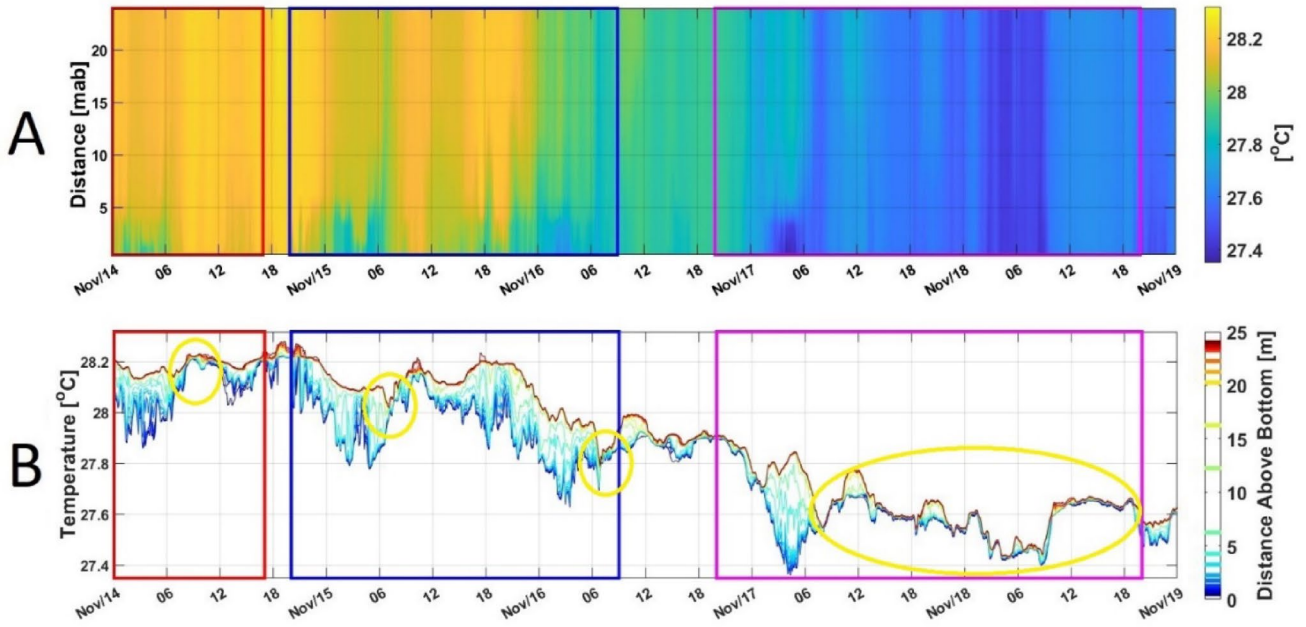

Fig. 6 Temperature chain time series from 18 temperature loggers, regular (2 Hz) and fast-response (16 Hz), attached to a tightly moored line. (**A**) Temperature contour plot and (**B**) temperature trace, where warmer-colored traces represent the shallow sensors, and cooler colors denote the deeper sensors. Data were averaged over 6-minute intervals. Yellow circles highlight periods with a homogeneous thermal structure. Red, blue, and magenta boxes indicate the periods of calm, pre-Shamal, and Shamal, respectively

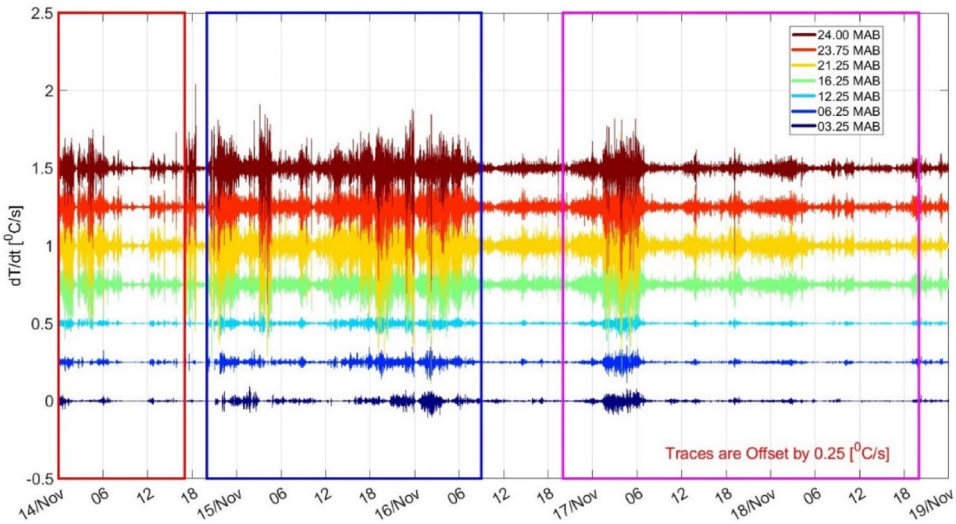

Fig. 7 Time series of temperature fluctuations from seven fast-response (16 Hz) temperature loggers attached to a tightly moored line, where warmer-colored traces represent the shallow sensors, and cooler colors denote the deeper sensors. Red, blue, and magenta boxes indicate the periods of calm, pre-Shamal, and Shamal, respectively

Moreover, temporal temperature fluctuations (Fig. 7) reveal distinct separation between surface and bottom during the morning, with higher fluctuations near the surface (24 MAB) and lower fluctuations near the seabed (3.25 MAB) as indicated by the higher ranges. This further emphasizes the presence of thermal layers. This also suggests that the relatively weak wind stress and low air-sea heat loss were too weak to destratify the water column. This is further supported by the small, less than 7.8 m, (green) and negative (orange) Monin-Obukhov length (Fig. 5B).

Further analysis of the spectrogram for both the surface (24 MAB; Fig. 8A) and bottom (3.5 MAB; Fig. 8B) sensors shows elevated spectral energy during the calm period following different cycles. The near seabed spectrogram and temperature variances (red) appear to roughly follow a semidiurnal cycle that was consistent with the tidal signal (for details see Al Senafi et al.,2020b; Li et al. 2020b), further emphasizing stratification and the insignificant contribution of atmospheric forcing near the seabed. In contrast, the near sea surface followed a diurnal cycle, with lower spectral levels and temperature variances observed during dawn, a period when the water column became more weakly stratified.

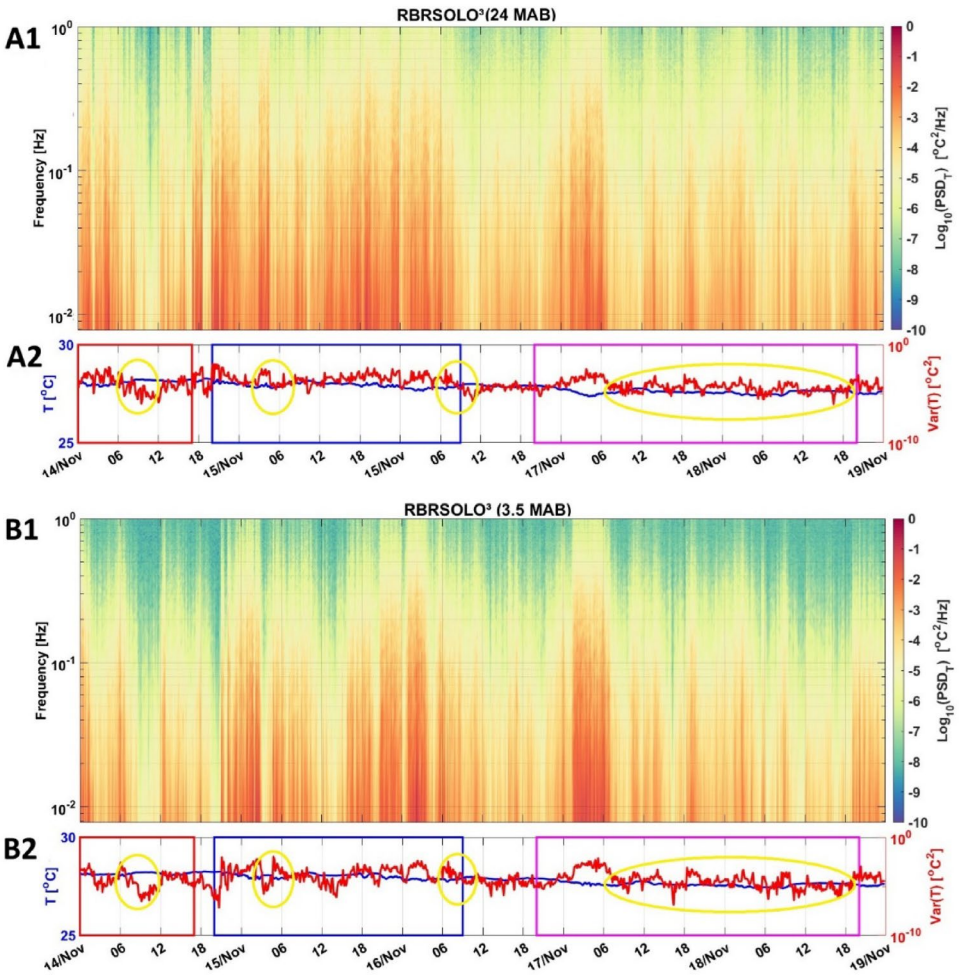

Fig. 8 Spectrogram of temperature fluctuations and temperature variances: (A1) Spectrogram computed from temperature time-series measured by a fast response temperature logger during a period of five days. (A2): temperature time-series trace (blue line) and temperature variance (red; log10 scale) computed for each FFT block. Temperature was sampled at 16 Hz and each FFT block includes 8192 samples (equivalent in time to ~9 min). The temperature logger was at 24 m above the bottom. (B1) and (B2) are similar to (A1) and (A2) but for temperature logger at 3.5 m above the bottom (nominal water depth 30.48 m). Yellow circles highlight periods of homogeneous thermal structure. The red, blue, and magenta boxes mark the periods of calm, pre Shamal, and Shamal, respectively

Interestingly, by morning between 6:00 and 12:00, the water column appeared to become more weakly stratified (Fig. 6B; yellow circle), with temperatures across the column differing by less than 0.01 °C and temperature fluctuations decreased from 0.1 °C/s to near zero (Fig. 7), indicating a homogeneous structure. The negative Monin-Obukhov length (Fig. 5B) suggests that buoyancy forces, rather than mechanical forces (wind stress), dominated, likely leading to convective mixing. However, by midday between 12:00 and 17:00, the column re-stratified, with temperature differences nearing 0.2 °C, and continued to increase toward the pre-Shamal period. The conditions observed during this calm period resulted in reduced mean ϵ and χ_T in the water column, with ϵ and χ_T values averaging 2.33×10^{-6} W/kg and 6.99×10^{-6} °C/s, respectively. These values are lower by more than an order of magnitude compared to the overall study period averages of 6.49×10^{-5} W/kg and 9.25×10^{-5} °C/s (Fig. 9A and B).

3.2 Pre-Shamal Period (November 15th To November 16th)

3.2.1 Atmospheric Conditions and Surface Fluxes

The pre-Shamal period marked an increase in atmospheric activity as winds shifted to the southeast, a precursor to the more intense Shamal winds. Hourly averaged wind speeds increased to 7.2 m/s (Fig. 4A), leading to a sharp rise in wind stress exceeding 0.1 N/m² (Fig. 5A). Although these squall winds fluctuated in intensity (between 1.1 and 7.2 m/s), they introduced a higher momentum flux to the ocean surface than during the calm period. The shift to southeasterly winds is typical of pre-Shamal conditions in the Gulf, driven by regional pressure gradients and the approaching high-pressure systems associated with Shamal events as detailed by Al Senafi and Anis (2015). This pattern was observed in the present study, which recorded a pressure increase from a minimum of 1012 mb during the pre-Shamal period to a maximum of 1019 mb during the Shamal event (Fig. 4B). These southeasterly winds, referred to as Kaus/Suahili winds, are commonly associated with cloudy

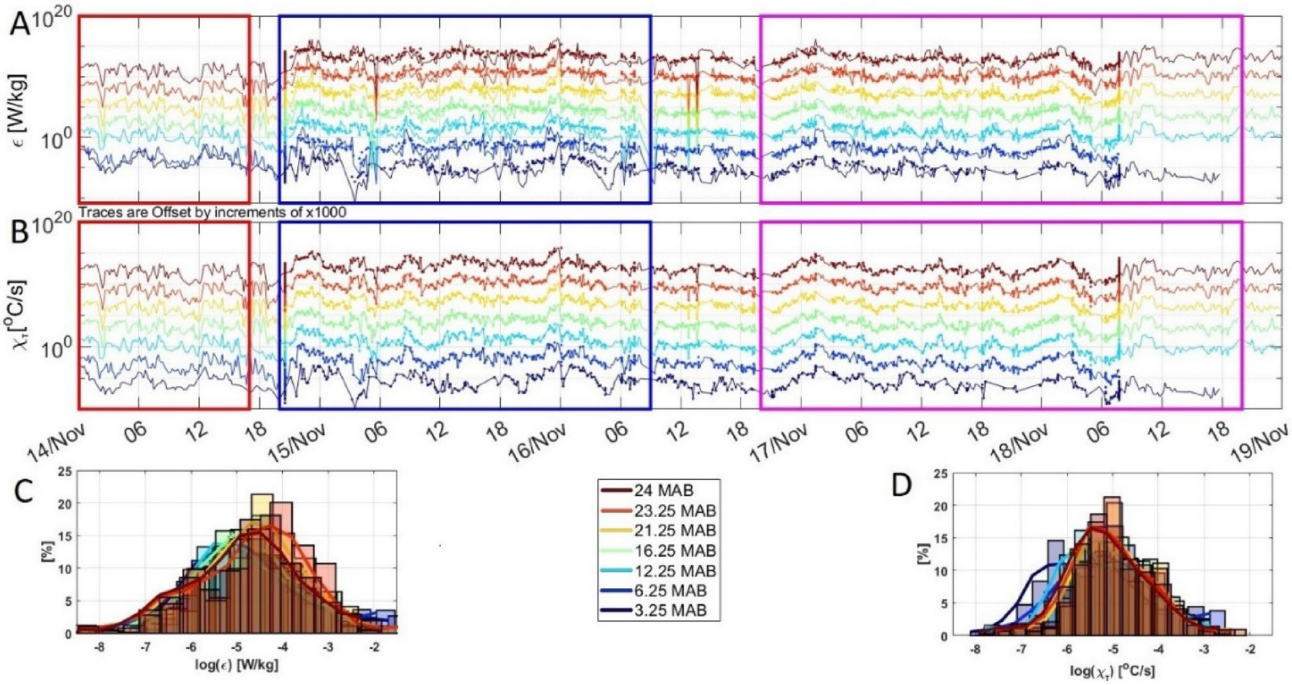

Fig. 9 Comparison of time series data from seven fast-response (16 Hz) temperature sensors used to estimate (**A**) ϵ and (**B**) χ_T, where warmer-colored traces represent the shallow sensors and cooler colors denote the deeper sensors. MicroCTD estimates of ϵ and χ_T at the nearest measurement point are shown as dots. Histograms display the distribution of estimates for (**C**) ϵ and (**D**) χ_T throughout the period. Red, blue, and magenta boxes indicate the periods of calm, pre-Shamal, and Shamal, respectively. No MicroCTD profiling was conducted during the calm period as profiling commenced late evening on 14th November and concluded late in the Shamal period, mid-day on 18th November. Panels A and B are offset by increments of ×1000 for visual clarity

conditions and squalls (Galvin and Membery 2008). Despite their regional significance, these winds are not extensively documented, and to the best of our knowledge, no detailed statistical analysis is available in the literature.

Heat fluxes during the pre-Shamal period showed increased energy exchange between the ocean and atmosphere. Latent heat flux rose significantly from near-zero levels at the end of the calm period, peaking at approximately 270 W/m² (Fig. 5E), indicating enhanced evaporation driven mainly by stronger winds. Sensible heat flux remained low, following a similar pattern to the calm period (Fig. 5D), due to low air-sea temperature contrast not exceeding 1.1 ˚C (Fig. 4C). The sky during this period was cloudy, as indicated by lower solar radiation compared to the previous day. Cloud cover increased downward longwave radiation, reducing net longwave radiation loss to a minimum of 40 W/m². The combined effects of lower solar radiation and higher latent heat flux resulted in continuous net heat loss, averaging 209 W/m² (Fig. 5F). However, despite the continuous heat loss and lower solar radiation being a third compared to the Shamal period, the average heat loss during pre-Shamal was less than the average heat loss of 242 W/m² observed during the following Shamal phase, likely due to the intermittent nature of the squall winds compared to the persistent Shamal winds and colder air temperatures.

3.2.2 Water Column Thermal Structure & Stability

As southeasterly winds developed during the pre-Shamal period, the temperature contour plot and sensor traces indicate the onset of surface cooling until dawn, though stratification persisted with water column temperature ranges exceeding 0.3 °C (Fig. 6B). The contour plot shows a slight cooling by 0.2 °C in the upper layers, with the warmer surface transitioning to cooler temperatures, particularly near the surface (Fig. 6A). The temperature traces similarly reflect this change, with the warmer surface sensors' temperatures beginning to converge with those of the cooler temperatures of the deeper sensors, especially within the upper 10 m. However, waters beneath this depth remained relatively unaffected, as indicated by the continued separation of temperature traces at depth.

By dawn, an increase in barometric pressure of 2.5 mb (Fig. 4B) within a period of two hours was observed, during which winds peaked at 7.1 m/s bringing cooler winds with temperatures below SST (Fig. 4C). These conditions led to a drop in SST driven mainly by the increase in wind stress and heat fluxes, particularly the rising latent heat flux, which peaked around 270 W/m² and accounted for 68% of the net heat flux loss. Stronger winds enhanced evaporation, cooling the surface and intensifying vertical mixing as

indicated by elevated fluctuations in temperature (Fig. 7), spectral levels and temperature variances (Fig. 8A), leading to a decrease in temperature differences across the column to less than 0.04 °C by the afternoon of November 15th (Fig. 6B; yellow circle). A period during which the average water column buoyancy frequency started to drop in half from 4 cph (Fig. 10A) and vertical current shear sharply increased from near 0 to 17 cph (Fig. 10B), further suggesting unstable conditions as indicated by the gradient Richardson number (Ri; Miles 1961) below the critical number ($Ri_c = 1$; Galperin et al. 2007) value (Fig. 10C, red). The Monin-Obukhov length increased during this time (Fig. 5B), indicating that mechanical forces (wind stress) were becoming more influential, compared to the buoyancy-driven processes dominant in the calm period. However, a brief wind weakening midday, due to the squall nature of these southeasterly winds, led to a decrease in shear from 17 cph to near zero and a tripling of buoyancy frequency from 2 cph, as well as re-establishment of stratification indicated by the Ri numbers above the critical value (Fig. 10C; green shading), with surface-to-bottom temperature differences near 0.4 °C (Fig. 6B).

Despite increased air-sea interactions by the midnight of November 16th, the wind was not strong enough to fully homogenize the surface and deeper layers, as indicated by lack of convergence of temperature traces as well as the higher than critical Ri number suggesting stability. However, by dawn of November 16th, the water column buoyancy frequency (Fig. 10A) and temperature range sharply reduced from 0.3 °C to less than 0.01 °C within just three hours, mirroring the mixing trend seen during the calm period. This suggests the dominance of buoyancy forces over mechanical forces, further supported by the smaller and negative Monin-Obukhov lengths (Fig. 5B). Despite the squall conditions and variable wind patterns described above, this period overall exhibited the highest fluctuations in temperature, reaching up to 0.9 °C/s (Fig. 7). These fluctuations were more persistent compared to the Shamal event, resulting in higher mean ϵ and χ_T in the water column, with ϵ and χ_T values averaging 1.13×10^{-4} W/kg and 1.76×10^{-4} °C/s, respectively. These values are higher compared to the Shamal period averages of 2.69×10^{-5} W/kg and 2.71×10^{-5} °C/s (Fig. 9A and B).

3.3 Shamal Period (November 16th To November 19th)

3.3.1 Atmospheric Conditions and Surface Fluxes

The Shamal period began in the evening of November 16th and was characterized by strong northwesterly winds which are typical of Shamal events in the Gulf. Wind speeds

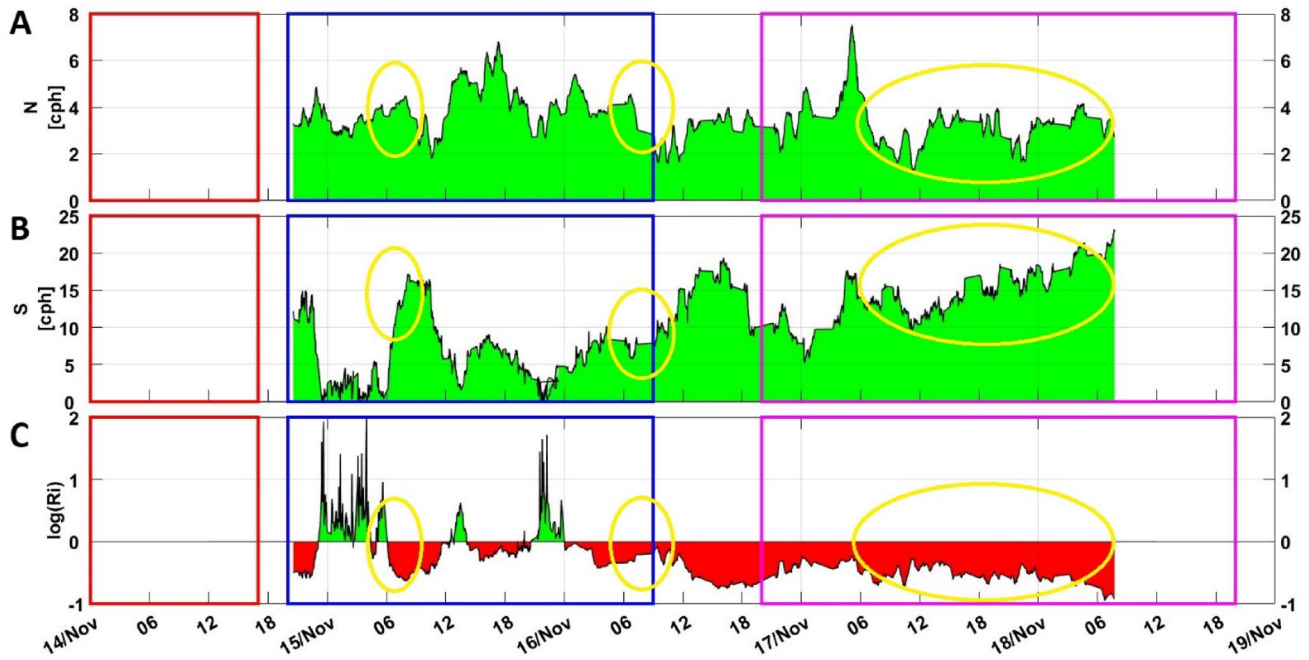

Fig. 10 MicroCTD measurements of: (**A**) buoyancy frequency, (**B**) velocity shear (calculated using the ADCP), and (**C**) the computed log scale gradient Richardson number, Ri. Red shading indicates values below the critical Ri number, suggesting vertical instability, while green shading denotes values above the critical Ri number, indicative of stable conditions. Yellow circles highlight periods with a homogeneous thermal structure. Red, blue, and magenta boxes mark the periods of calm, pre-Shamal, and Shamal, respectively. No MicroCTD profiling was conducted during the calm period, as profiling began late evening on the 14th of November and concluded mid-day on the 18th November, during the Shamal period

exceeded 5 m/s, with hourly averaged peaks approaching 7.5 m/s (Fig. 4A), resulted in a significant increase in wind stress, peaking around 0.1 N/m² (Fig. 5A). These strong winds, with single-minute observations reaching up to 11.3 m/s, were driven by the interaction between high-pressure systems over the Arabian Peninsula with lower pressure systems to the southeast, generating strong pressure gradients (Vishkaee et al. 2012). The Shamal event reported in the present study is ranked in the 55th percentile in wind strength compared to the 421 documented Shamal events reported by Al Senafi and Anis (2015) over a 40-year period. These winds significantly enhanced air-sea interactions resulting in enhanced mixing which is examined below.

During the Shamal period, latent heat flux nearly doubled, reaching 290 W/m² compared to the 151 W/m² observed at the beginning of this period (Fig. 5E), reflecting high evaporation rates driven by intensifying winds. The cooler and drier land-originating northwesterly winds lowered humidity levels and increased the air-sea humidity gradient, further enhancing moisture flux from the ocean surface. Sensible heat flux increased to 55 W/m², accounting for 15% of the total heat flux loss (Fig. 5D), due to the stronger winds and larger air-sea temperature differences as cooler Shamal winds moved over the relatively warm ocean surface (Fig. 4C).

The net heat flux during the Shamal event became strongly negative, indicating substantial heat loss from the ocean to the atmosphere, with a peak loss of 418 W/m², compared to the peak loss during the pre-Shamal period of 321 W/m². This heat loss was primarily driven by the sharp increase in latent heat flux, which accounted for 59% of net heat loss, and was followed by longwave radiation losses contributing 23% (Fig. 5C). Reduced shortwave radiation (Fig. 5B) likely resulted from the presence of both dust and clouds, common during Shamal events (Thoppil and Hogan 2010; Abadi et al. 2022). The proportion of heat flux losses due to latent, sensible, and longwave radiation is consistent with the range of a typical "fingerprint" of a winter Shamal event, as characterized by Al Senafi et al. (2019).

These air-sea heat flux observations are consistent with those of Li et al. (2020a), who analyzed the Gulf's response to a three-day winter Shamal event. Their study showed that air-sea heat losses increased sixfold during the event, which is comparable to our observations of a fivefold increase compared to the calm period.

3.3.2 Water Column Thermal Structure & Stability

The Shamal period introduced significant changes to the thermal structure of the water column. The strong northwesterly winds drove intense surface cooling and vertical mixing, fundamentally altering the water column's stratification. The temperature contour plot shows a rapid shift from warmer tones (yellow and green) to cooler ones (blue), indicating uniform cooling from the surface to the bottom (Fig. 6A). This cooling was particularly pronounced on November 18th, when temperatures at all depths converged around 27.4 °C, as depicted by the dominance of dark blue tones in the contour plot.

The temperature traces further highlight this mixing. During the Shamal, the initially well-separated traces during dawn of November 17th, with a temperature difference of 0.47 °C between surface and bottom, converged within 3.5 h (Fig. 6B; highlighted by the yellow circle). During this 3.5-hour period, a burst of elevated fluctuations in temperature of up to 0.8 °C/s was observed (Fig. 7). This was closely followed by higher mean TKE and temperature dissipation rates near the surface, with ϵ and χ_T values averaging 8.45×10^{-4} W/kg and 6.51×10^{-4} °C/s, respectively (Fig. 9A & B). The temperature differences following this 3.5-hour episode remained below 0.1 °C throughout the Shamal period, signifying a more weakly stratified water column from surface to bottom. The rapid cooling and homogeneity in temperature was likely driven by both the intense, continuous, wind stress (Fig. 5A) and the significant latent heat flux (Fig. 5E). The Monin-Obukhov length scale remains predominantly negative throughout the intensification of Shamal winds (Fig. 5B), suggesting that surface cooling and convective overturning continue to dominate the turbulent dynamics. This pattern can be attributed to the strong net surface heat loss caused by cold, dry air masses accompanying the Shamal, which significantly amplifies buoyancy-driven mixing. While wind stress increases during this period, the rapid rate of surface cooling exceeds the mechanical input, leading to a sustained convective regime. This interpretation aligns with prior studies (e.g. Li et al. 2020a) in the Gulf that highlight the importance of buoyancy forcing during winter events.

Despite the differences in spectral levels (Figs. 7A1 & B1) and temperature variances (Figs. 7A2 & B2) between the near-surface and near-bottom sensors, the pattern remained consistent, with a significant correlation of 0.68 during this period between the temperature variance signals, signifying a homogenous water column, compared to insignificant (near 0) correlation values during the previous two periods. In addition, the dominant role of vertical current shear led to Ri numbers below the critical threshold, further indicating instability (Fig. 10).

Table 1 Comparison of Turbulent Kinetic Energy Dissipation (ϵ) and Temperature Dissipation (χ_T) estimates from RBRsolo³ T sensors and our benchmark profiler MicroCTD. (A) ϵ estimates (log scale), (B) χ_T estimates (log scale). The tables display averages and 95% confidence intervals (in parentheses) for RBRsolo³ T and MicroCTD at different depths. Error percentage indicates the difference between RBRsolo³ T and the benchmark profiler at each depth

(A) Turbulent Kinetic Energy Dissipation (ϵ)			
Depth	RBR*solo*³ T Log [W/kg]	MicroCTD Log [W/kg]	Error
24 MAB	-4.11 (-4.31, -3.72)	-4.24 (-4.32, -4.14)	-3%
23.25 MAB	-4.19 (-4.43, -3.96)	-4.26 (-4.26, -4.10)	-2%
21.25 MAB	-4.37 (-4.73, -3.83)	-4.65 (-4.99, -4.10)	-6%
16.25 MAB	-4.75 (-4.92, -4.50)	-5.21 (-5.38, -5.13)	-9%
12.25 MAB	-5.04 (-5.50, -4.70)	-5.11 (-5.28, -5.05)	-2%
6.25 MAB	-5.08 (-5.81, -4.91)	-5.18 (-5.35, -5.08)	-2%
3.25 MAB	-5.60 (-5.75, -5.37)	-6.19 (-6.37, -6.05)	-10%

(B) Temperature Dissipation (χ_T)			
Depth	RBR*solo*³ T Log [°C²/s]	MicroCTD Log [°C²/s]	Error
24 MAB	-5.09 (-5.27, -4.81)	-5.18 (-5.34, -4.96)	18%
23.25 MAB	-4.95 (-5.09, -4.80)	-5.00 (-5.15,-4.84)	11%
21.25 MAB	-5.05 (-5.19, -4.85)	-5.11 (-5.26, -4.91)	12%
16.25 MAB	-5.09 (-5.25, -4.85)	-5.15 (-5.30, -4.85)	13%
12.25 MAB	-5.82 (-6.06, -5.45)	-5.88 (-6.11, -5.85)	12%
6.25 MAB	-5.89 (-6.15, -5.45)	-5.94 (-6.20, -5.48)	11%
3.25 MAB	-6.02 (-6.20, -5.78)	-6.07 (-6.25, -5.83)	11%

3.4 Comparison of RBR*solo*³ T Sensors and Turbulence Profilers Estimating of Turbulent Kinetic Energy Dissipation (ϵ) and Temperature Dissipation (χ_T)

Figure 9 presents a detailed comparison between two methods of measuring marine turbulence properties: a MicroCTD turbulence profiler (used here as the benchmark) and our new method of using moored fast-response temperature sensors (RBR*solo*³ T). Our comparison focuses on two key turbulence parameters ϵ and χ_T. Both methods produced comparable results, demonstrating strong agreement in their estimates across different time periods and depths.

The time series of ϵ (Fig. 9A) reveals that the RBR*solo*³ T sensors captured the overall turbulence patterns well, closely aligning with those of the MicroCTD across all six depth levels, which are represented by a blue-to-red color gradient, particularly during the enhanced turbulence periods of pre-Shamal and Shamal. For example, during the Shamal period, RBR*solo*³ T estimates at 24 MAB (red) ranged from 10^{-6} to 10^{-4} W/kg, closely matching the MicroCTD data range. This suggests that the RBR*solo*³ T method allows accurate tracking of increases in mixing intensities, here driven by wind stress and convection.

The histograms of ϵ values (Fig. 9C) further support the agreement between the two methods. The RBR*solo*³ T sensors (color bars) produce estimates within a similar range to the MicroCTD (color lines) measurements, especially during periods of strong wind forcing like the Shamal. The shallow sensors, exhibited higher ϵ values (average of 10^{-5} W/kg), reflecting the influence of wind-driven turbulence, while the deeper sensors showed lower values (down to 10^{-6} W/kg). The average ϵ values from Table 1 A show that during the pre-Shamal and Shamal periods, estimates from both methods remain within a margin of error between 2 and 10% across all depths. For example, during the Shamal period at 24 MAB, the RBR*solo*³ T estimates average of ϵ was 3.1×10^{-5} W/kg, while that of the MicroCTD was 3.5×10^{-5} W/kg. Correlation values between the RBR*solo*³ T and MicroCTD methods averaged 0.64, and up to 0.68 during periods of increased wind stress.

Similarly, time series of χ_T (Fig. 9B) showed that the RBR*solo*³ T method tracks the MicroCTD measurements well, capturing the temperature dissipation dynamics well, particularly during periods of strong wind forcing. For instance, during the Shamal period, the RBR*solo*³ T and MicroCTD estimates of χ_T at 24 MAB ranged from 10^{-7} to 10^{-5} °C²/s and demonstrated a similar response to enhanced turbulence and mixing. During the calm period, the RBR*solo*³ T reported consistently relatively low values for χ_T, averaging ~ 10^{-7} °C²/s, consistent with stable conditions and minimal mixing.

The histograms of χ_T values (Fig. 9D) illustrate that the RBR*solo*³ T method produces distributions that align closely with those of the MicroCTD, especially during the turbulent Shamal period. Like ϵ, the shallow sensors show higher χ_T values (e.g., average ~ 10^{-6} °C²/s), while deeper sensors reflect lower dissipation rates (down to ~ 10^{-7}

°C²/s). Table 1B data confirms that the differences between the RBR*solo*³ T and MicroCTD estimates for χ_T were generally small (within 11–18%). For example, during the Shamal period at 12.25 MAB, the RBR*solo*³ T method estimated χ_T as 2.42×10^{-6} °C²/s, while that of the MicroCTD as 2.16×10^{-6} °C²/s, again showing a good match.

4 Conclusions

This study has provided a comprehensive analysis of the effects of winter Shamal events on water column mixing and turbulence in the northern Gulf, using a newly developed method for computing turbulence properties (ϵ and χ_T). By utilizing fast-response temperature sensors and turbulence profiling, we captured the dynamics of turbulent mixing during Shamal events, which were shown to be key drivers of enhanced water column mixing. Our findings demonstrate that Shamal-induced turbulence plays a critical role in air-sea exchanges of momentum and heat. The strong, cold winds associated with Shamal events lead to intense wind-driven mixing and convection, which may significantly influence the Gulf's ecological systems. The results provide the one of the first observational analysis of the direct response of water column turbulence to Shamal forcing, offering key insights into the broader implications of atmospheric events for Gulf dynamics.

In addition to Shamal events, the study also highlighted the contrasting conditions during the calm periods and the pre-Shamal phase, which was characterized by squall-like southeasterly winds. Despite being less persistent than Shamal winds, the pre-Shamal southeasterly winds introduced intermittent bursts of stronger wind, leading to periods of enhanced mixing. These squalls demonstrate how varying atmospheric conditions—ranging from calm to intense squall winds—differentially impact the thermal and turbulence structure of the Gulf. By observing these varying conditions, we were able to distinguish between the relatively low mixing intensities during calm periods and the more intense dynamics driven by both Shamal events and pre-Shamal squalls, providing a broader understanding of the Gulf's response to atmospheric forcing.

While this work presents a significant advancement in measuring and understanding the impacts of winter Shamal events on Gulf turbulence, further development is planned. Future work will focus on the publication of a technical paper that outlines the detailed methodology adapted to this new approach. Additionally, we will release a MATLAB toolbox based on the new method. This toolbox will serve as a valuable resource for oceanographers and researchers, enabling wider application of this innovative approach in future investigations of ocean turbulence.

Acknowledgements We thank the Kuwaiti Coast Guard for providing field logistics, transportation and divers. We also thank the undergraduate students from the Marine Science Department at Kuwait University for their invaluable assistance in the field. Special thanks are extended to Mr. Yusuf Bohadi, Mr. Abdulhadi Esmail, and Mr. Mostafa Omar for their dedicated contributions in the field. Additionally, we are grateful to Ms. Noor Al Fayez for her expertise in the schematic design of the experimental setup. We also thank Dr. Hala Al Jassar from the Physics Department at Kuwait University for providing access to satellite imagery. The KuwaitSat-1 image used in the graphical abstract was obtained through Project #FP-18-14-SP-01, which was supported by funding from the KFAS.

Authors Contribution Fahad Al Senafi: Writing – original draft, review & editing, Project administration, Supervision, Methodology, Investigation, Formal analysis, Visualization, Conceptualization, Funding acquisition. Ayal Anis: Writing – review & editing, Methodology, Formal analysis, Conceptualization. Tariq Al Rushaid: Writing – review & editing, Formal analysis, Investigation, Funding acquisition. Sebastiano Piccolroaz: Writing – review & editing, Methodology, Formal analysis.

Funding This project was funded by both Kuwait Foundation for the Advancement of Sciences (KFAS) under project code: CN21-44SE-1369 and the Research Sector at Kuwait University (KU) under project code: RX-01/21.

Data Availability Data will be made available on request.

Declarations

Competing Interest The authors declare that they have no known competing financial interests or personal relationships that could have appeared to influence the work reported in this paper.

References

Abadi ARS, Hamzeh NH, Chel Gee Ooi M, Kong SS-K, Opp C (2022) Investigation of two severe Shamal dust storms and the highest dust frequencies in the south and southwest of Iran. Atmosphere 13:1990. https://doi.org/10.3390/atmos13121990

Aboobacker VM, Vethamony P, Rashmi R (2011) Shamal" swells in the Arabian Sea and their influence along the west coast of India. Geophys Res Lett. https://doi.org/10.1029/2010GL045736

Al Senafi F, Anis A (2015) Shamals and climate variability in the Northern Arabian Gulf from 1973 to 2012. Int J Climatol. https://doi.org/10.1002/joc.4247

Al Senafi F, Anis A, Menezes V (2019) Surface heat fluxes over the Northern Arabian Gulf and the Northern red sea: evaluation of ECMWF-ERA5 and NASA-MERRA2 reanalyses. Atmosphere 10(9):505. https://doi.org/10.3390/atmos10090505

Al Senafi F, Anis A (2020a) Wind-driven flow dynamics off the Northwestern Arabian Gulf Coast. Estuar Coast Shelf Sci 233:106511. https://doi.org/10.1016/j.ecss.2019.106511

Al Senafi FA, Abed RMM, Muthukrishnan T, Anis A, Mahmoud H (2020b) Development and diversity of bacterial biofilms in response to internal tides: A case study off the Coast of Kuwait. Front Mar Sci 7:1–13. https://doi.org/10.3389/fmars.2020.00107

Al Senafi F, Rushaid A, T., Al Mukaimi M (2024) Climate variability of air temperature and its warming trends in the Arabian Gulf. Atmosphere 8:587–598. https://doi.org/10.3390/atmos13040587

Anis A (2006) Similarity relationships in the unstable aquatic surface layer. Geophys Res Lett 33:L19609. https://doi.org/10.1029/2006GL027082

Attrill MJ (2009) Sea temperature change as an indicator of global change. In: Letcher TM (ed) Climate change. Elsevier, Amsterdam, pp 337–347

Ben-Hasan A (2024) Trends in Marine Fisheries of the Arabian/Persian Gulf. In Oceanographic and Marine Environmental Studies around the Arabian Peninsula, edited by N. M. A. Rasul and I. C. F. Stewart, 197–205. CRC Press

Ben-Hasan A, Walters C, Christensen V, Al-Husaini M, Al-Foudari H (2018) Is reduced freshwater flow in Tigris-Euphrates rivers driving fish recruitment changes in the Northwestern Arabian gulf? Mar Pollut Bull 129:1–7. https://doi.org/10.1016/j.marpolbul.2018.01.003

Blain CA (2000) Modeling three-dimensional thermohaline-driven circulation in the Arabian Gulf. In M. L. Spaulding & H. L Butler (Eds.), Proceedings of the 6th International Conference on Estuarine and Coastal Modeling (pp. 74–93). ASCE, Reston, VA

Brook MC, Houqani A, H., Al Mugrin A (2006) The current status and future requirements of water resources management in the Arabian Peninsula. In: Amer KM, Boer B, Brook MC, Adeel Z (eds) Policy perspectives for ecosystem and water management in the Arabian Peninsula. UNU-INWEH. 117p

Bruciaferri D, Tonani M, Ascione I, Al Senafi F, O'Dea E, Hewitt HT, Saulter A (2022) GULF18, a high-resolution NEMO-based tidal ocean model of the Arabian/Persian Gulf. Geosci Model Dev 15(23):8705–8730. https://doi.org/10.5194/gmd-15-8705-2022

Cheng NS, Wei MX, Chiew YM, Lu YS, Emadzadeh A (2020) Combined effects of mean flow and turbulence on sediment pickup rate. J Hydraul Res. https://doi.org/10.1080/00221686.2022.2064373

Danaila L, Antonia RA (2009) Spectrum of a passive scalar in moderate Reynolds number homogeneous isotropic turbulence. Phys Fluids 21(11):111702. https://doi.org/10.1063/1.3253819

Emery WJ, Thomson RE (2004) Data Analysis Methods in Physical Oceanography, 2nd ed. Elsevier, Amsterdam

Fairall C, Bradley E, Rogers D, Edson J, Young G (1996) Bulk parameterization of air-sea fluxes for TOGA COARE. J Phys Res 101:3747–3764. https://doi.org/10.1029/95JC03205

Fairall C, Bradley E, Hare J, Grachev A, Edson J (2003) Bulk parameterization of air-sea fluxes: updates and verification for the COARE algorithm. J Clim 16(4):571–591. https://doi.org/10.1175/1520-0442(2003)016

Fieseler CM, Al-Mudaffar Fawzi N, Helmuth B, Leitão A, al, Ainsi M, al, Mukaimi M, Al-Saidi M, al, Senafi F, Bejarano I, Ben-Hamadou R, D'Addario J et al (2023) Expanding ocean protection and peace: A window for science diplomacy in the Gulf. Royal Soc Open Sci 10(9). https://doi.org/10.1098/rsos.230435

Galperin B, Sukoriansky S, Anderson PS (2007) On the critical Richardson number in stably stratified turbulence. Atmos Sci Lett 8:65–69. https://doi.org/10.1002/asl.153

Galvin JFP, Membery DA (2008) The weather and climate of the tropics: part 5 - Dry environments. Weather 63(3):100–106. https://doi.org/10.1002/wea.230

Gregg MC, Meagher TB (1980) The dynamic response of glass rod thermistors. J Geophys Res 85(C5):2779–2786. https://doi.org/10.1029/JC085iC05p02779

Halverson M, Jackson J, Richards C, Melling H, Brunsting R, Dempsey M et al (2017) Guidelines for processing RBR CTD profiles. Canadian Technical Report of Hydrography and Ocean Sciences, 314. Retrieved from https://waves-vagues.dfo-mpo.gc.ca/Library/40578112.pdf

Hill RJ (1978) Models of the scalar spectrum for turbulent advection. J Fluid Mech 88(3):541–562. https://doi.org/10.1017/S002211207800227X

Keller D, Givon Y, Pennel R, Raveh-Rubin S, Drobinski P (2024) Untangling the mistral and seasonal atmospheric forcing driving deep convection in the Gulf of Lion: 1993–2013. J Geophys Res Oceans 129:202400234. https://doi.org/10.1029/2023JC020234

Kerr RM (1990) Velocity, scalar and transfer spectra in numerical turbulence. J Fluid Mech 211:309–332. https://doi.org/10.1017/S0022112090001586

Kraichnan R (1968) Small-scale structure of a scalar field convected by turbulence. Phys Fluids 11(5):945–953. https://doi.org/10.1063/1.1692063

Kundu P, Cohen IM (2012) Fluid mechanics, 5th edn. Elsevier

Lee CM et al (2005) Northern Adriatic response to a wintertime Bora wind event. Eos. Trans Am Geophys Union 86(16):157–164. https://doi.org/10.1029/2005EO160002

Li D, Anis A, Al Senafi F (2020a) Physical response of the Northern Arabian Gulf to winter Shamals. J Mar Syst 203:103270. https://doi.org/10.1016/j.jmarsys.2019.103270

Li D, Anis A, Al Senafi F (2020b) Neap-spring variability of tidal dynamics in the Northern Arabian Gulf. Cont Shelf Res 197:104086. https://doi.org/10.1016/j.csr.2019.104086

Miles JW (1961) On the stability of heterogeneous shear flows. J Fluid Mech 10(4):496–508. https://doi.org/10.1017/S0022112061000305

Mirza MQ (2002) Global warming and changes in the probability of occurrence of floods in Bangladesh and implications. Glob Environ Change 12(2):127–138. https://doi.org/10.1016/S0959-3780(02)00002-X

Monin AS, Obukhov AM (1954) Basic laws of turbulent mixing in the surface layer of the atmosphere. Tr Geofiz Inst Akad Nauk SSSR 24:163–187

Moum JN, Nash JD (2009) Mixing measurements on an Equatorial ocean mooring. J Atmos Ocean Technol 26:317–336

Nash JD, Caldwell DR, Zelman MJ, Moum JN (1999) A thermocouple probe for high-speed temperature measurement in the Ocean. J Atmos Oceanic Technol 16:1474–1482. https://doi.org/10.1175/1520-0426(1999)016<1474:ATPFHS>2.0.CO;2

Osborn TR (1980) Estimates of the local rate of vertical diffusion from dissipation measurements. J Phys Oceanogr 10:83–89. https://doi.org/10.1175/1520-0485(1980)010<0083:EOTLRO>2.0.CO;2

Osborn TR, Cox CS (1972) Oceanic fine structure. Geophys Fluid Dyn 3(4):321–345. https://doi.org/10.1080/03091927208236085

Piccolroaz S, Fernández-Castro B, Toffolon M et al (2021) A multi-site, year-round turbulence microstructure atlas for the deep Perialpine lake Garda. Sci Data 8:188. https://doi.org/10.1038/s41597-021-00965-0

Portwood GD, de Bruyn Kops SM, Caulfield CP (2022) Implications of inertial subrange scaling for stably stratified mixing. J Fluid Mech 939:10. https://doi.org/10.1017/jfm.2022.160

Ragessi IM, García CM, Damian SM, Tarrab L, Patalano A, Rodriguez A (2022) Detailed experimental and numerical analysis of hydrodynamics in the outflow measurement channel of a sewage

treatment plant. J Hydroinformatics 24(4):798–817. https://doi.org/10.2166/hydro.2022.055
Rao PG, Al-Sulaiti M, Al-Mulla AH (2001) Winter Shamals in Qatar, Arabian Gulf. Weather 56:444–451. https://doi.org/10.1002/j.1477-8696.2001.tb06532.x
Rao PG, Hatwar HR, Al-Sulaiti M, Al-Mulla AH (2003) Summer Shamals over the Arabian Gulf. Weather 58:471–478. https://doi.org/10.1002/wea.662
Ruddick B, Anis A, Thompson K (2000) Maximum likelihood spectral fitting: the Batchelor spectrum. J Atmos Ocean Technol 17(11):1541–1555. https://doi.org/10.1175/1520-0426(2000)017
Sreenivasan KR (1995) On the universality of the Kolmogorov constant. Phys Fluids 7(11):2778–2784. https://doi.org/10.1063/1.868656
Sreenivasan KR (1996) The passive scalar spectrum and the Obukhov-Corrsin constant. Phys Fluids 8(1):189–196. https://doi.org/10.1063/1.868768
Sullivan JM, Swift E, Donaghay PL, Rines JEB (2003) Small-scale turbulence affects the division rate and morphology of two red-tide dinoflagellates. Harmful Algae 2(3):183–199. https://doi.org/10.1016/S1568-9883(03)00026-5
Sutherland BR, Dibenedetto M, Kaminski A, van den Bremer T (2023) Fluid dynamics challenges in predicting plastic pollution transport in the ocean: a perspective. Phys Rev Fluids 8(7):070701. https://doi.org/10.1103/PhysRevFluids.8.070701
Swift SA, Bower AS (2003) Formation and circulation of dense water in the Persian/Arabian Gulf. J Geophys Res 108(C1):3004. https://doi.org/10.1029/2002JC001360
Tagawa K, Kato Y, Ohta (2003) Response compensation of thermistors: frequency response and identification of thermal time constant. Rev Sci Instrum 1 March 74(3):1350–1358. https://doi.org/10.1063/1.1542668
Thoppil PG, Hogan PJ (2010) Persian Gulf response to a wintertime Shamal wind event. Deep-Sea Res Part I Oceanogr Res Papers 57(8):946–955. https://doi.org/10.1016/j.dsr.2010.05.012
van Vliet MTH, Franssen WHP, Yearsley JR, Ludwig F, Haddeland I, Lettenmaier DP, Kabat P (2013) Global river discharge and water temperature under climate change. Glob Environ Change 23(2):450–464. https://doi.org/10.1016/j.gloenvcha.2012.11.002
Vishkaee F, Flamant C, Cuesta J, Oolman L, Flamant P, Khalesifard HR (2012) Dust transport over Iraq and northwest Iran associated with winter Shamal: a case study. J Geophys Res Atmos 117(D3):D03201. https://doi.org/10.1029/2011JD016339
Yang D, Chen B, Chamecki M, Meneveau C (2015) Oil plumes and dispersion in Langmuir, upper-ocean turbulence: large-eddy simulations and K-profile parameterization. J Geophys Res Oceans 120(7):4729–4759. https://doi.org/10.1002/2014JC010542